FULL PAPER

The relation between the surface composition anomaly and distribution of the exosphere of Mercury

Yudai Suzuki[1*] , Kazuo Yoshioka[2], Go Murakami[1] and Ichiro Yoshikawa[2]

Abstract

In celestial bodies with tenuous collisionless atmospheres, such as Mercury, the spatial distribution of the exosphere is expected to reflect the surface composition. In this study, we discuss whether the distributions of Mg, Ca, and Na, the primary exospheric components of Mercury, have a local exosphere–surface correlation by analyzing the observation data of the Mercury Atmospheric and Surface Composition Spectrometer (MASCS) and X-ray spectrometer (XRS) onboard the MErcury Surface, Space ENvironment, GEochemistry, and Ranging (MESSENGER) spacecraft. It was found that Mg has a strong local exosphere–surface correlation and Ca has a weak correlation. The Monte Carlo simulations of trajectories in the exosphere show that the weak correlation of Ca is due to the relatively large solar radiation acceleration. In addition, Na production rate in high-temperature regions is longitudinally dependent. This can be explained by considering that the weakly physisorbed Na layer on the surface is depleted under high temperature and that the distribution of strongly chemisorbed Na atoms is reflected in the exosphere. Based on these results, the conditions for components with a correlation in celestial bodies with thin atmospheres may include low volatility and low solar radiation acceleration.

Keywords Mercury, Surface-bounded exosphere, Surface composition, MESSENGER, BepiColombo
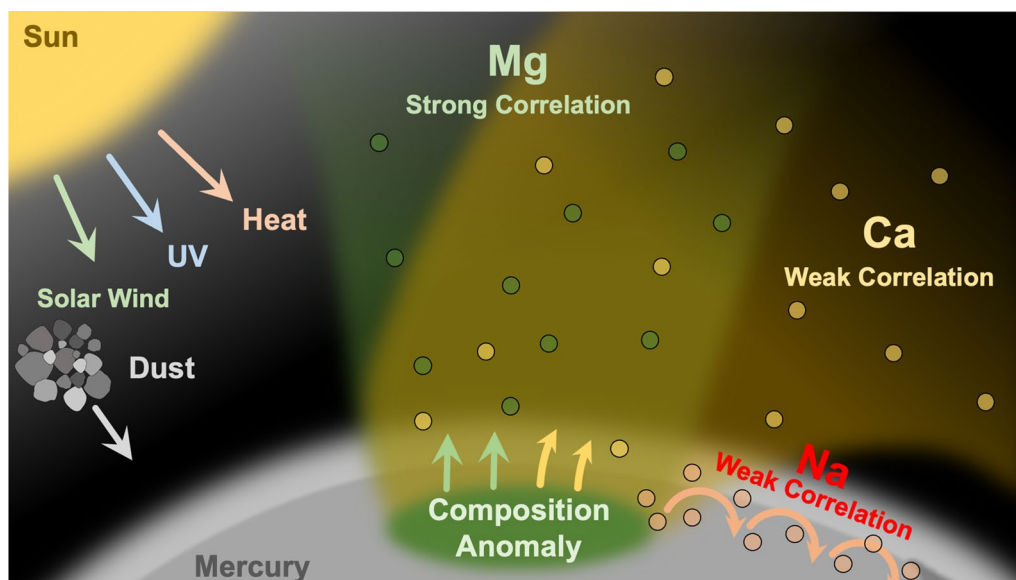
*Correspondence:
Yudai Suzuki
suzuki.yudai@jaxa.jp
Full list of author information is available at the end of the article

Suzuki *et al. Earth, Planets and Space*   (2023) 75:174

Page 2 of 12

Graphical Abstract

Introduction

Many celestial bodies in our solar system, such as Mercury, most moons, comets, and asteroids, have thin and collisionless atmospheres called exospheres. Most of these atmospheres are directly supplied from the surface through several processes, such as thermal desorption, photo-stimulated desorption (PSD), charged particle sputtering (CPS), and micro-meteoroid impact vaporization (MIV). The spatial structure of thin atmospheres strongly depends on their surface composition and energy distribution when released. Because the surface distribution of some components corresponds to resurfacing histories caused by volcanic activities, it is expected that the structure of the exospheres can be directly linked to them. The amount of potassium (K) in the exosphere on the Moon has been reported to increase over the potassium, rare-earth elements, and phosphorous (KREEP) regions (Colaprete et al. 2016; Rosborough et al. 2019). The surface composition distribution and volcanic histories of some planets with thin atmospheres can be estimated using remote atmospheric observations.

Magnesium (Mg) in the exosphere is thought to be ejected from the surface mainly through MIV, because observations by the Mercury Atmospheric and Surface Composition Spectrometer (MASCS; McClintock and Lankton 2007) onboard the MErcury Surface, Space ENvironment, GEochemistry, and Ranging (MESSENGER) spacecraft show that the Mg exosphere consists of high-energy atoms and has strong dawn-dusk asymmetry

(Merkel et al. 2017). The surface Mg density distribution was obtained using the X-ray spectrometer (XRS; Schlemm II et al., 2007) onboard MESSENGER. XRS revealed that Mg concentrates on the terrain between −120ºE and −80ºE in the Northern Hemisphere (Weider et al. 2015). Merkel et al. (2018) compared MASCS data with XRS data and carefully removed the dependency on true anomaly angle (TAA) and local time. They indicated that the enhanced production rate of the Mg exosphere can be seen above this high-Mg region. This is an interesting example of the local exosphere–surface correlation on Mercury identified from observations.

In addition, calcium (Ca) is also mainly ejected through MIV (Burger et al. 2014). Killen and Hahn (2015) and Christou et al. (2015) suggested that the impact of comet dust streams also contributes to the ejection of Ca exosphere during some seasons. The surface Ca distribution is known to be similar to that of Mg based on the observations by XRS (Weider et al. 2015; Nittler et al. 2020). Ca is qualitatively expected to have an exosphere–surface correlation along with Mg, because both Ca and Mg are refractory components and are mainly ejected by MIV. However, an exosphere–surface correlation on Ca has not been discussed yet.

The sodium (Na) exosphere is now divided into two components: a lower-energy component ejected through PSD and a higher-energy component ejected through MIV or CPS (Cassidy et al. 2015). The seasonal variability of the Na exosphere has been discussed in several

model studies, such as Mura et al. (2009) and Leblanc and Johnson (2010). Although no thermal components have been detected in the exosphere, surface Na in high-temperature regions has been said to be depleted owing to thermal desorption. This is supported by the fact that the amount of the exospheric Na at lower altitude does not reach maximum at perihelion (Cassidy et al. 2015). Cassidy et al. (2016) found that the amount of exospheric sodium was enhanced at specific "cold-pole" longitudes (around ±90°E) throughout the Mercury year. They attributed this phenomenon to the fact that the maximum temperature at these longitudes is the lowest on Mercury owing to the spin–orbit resonance. In contrast, Suzuki et al. (2020) suggested that additional Na ejection and supply of Na by dust streams' impact on these regions is also important for the enhancement, and Sarantos and Tsavachidis (2020) indicated that diffusion into the regolith also controls the amount of desorption. Besides, Killen et al. (2022) showed that Na ejected through CPS may be more energetic and contribute more to escape than conventional understanding. The cause of the seasonal variability of the Na exosphere remains as a big problem. If the surface Na distribution is highly temperature-dependent, the distribution of exospheric Na may not directly reflect volcanic histories.

In this study, we verified whether Mg, Ca, and Na on Mercury actually exhibited local surface–exosphere correlations using observational data from the MASCS and XRS onboard MESSENGER to understand the relationship between the distribution of the exosphere and that of the surface composition of celestial bodies with thin atmospheres. For Mg, our analysis is not significantly different from Merkel et al. (2018) and its main purpose is as a reference for confirming our methods.

Observations by MASCS/UVVS and XRS onboard messenger

The MESSENGER spacecraft, launched in 2004, orbited Mercury from 2011 to 2015 for approximately 17 Mercury years. In this study, we used the Ultraviolet and Visible Spectrometer (UVVS) channel of MASCS to estimate production rates of exospheric atoms, as well as XRS for the calculation of surface abundance.

UVVS channel of MASCS

MASCS consists of two channels: UVVS and the Visible and Infrared Spectrometer (VIRS). UVVS, a grating monochromator, scans narrow wavelength ranges around resonance-scattering emission lines of several atoms. Mg, Ca, and Na spectral scans cover 283.4–287.2 nm, 421.1–424.4 nm, and 587.7–591.1 nm with 0.2 nm step size, which include MgI (285.2 nm), CaI (422.7 nm), and NaI D1 (589.8 nm) and D2 (589.1 nm), respectively.

Owing to the northward line-of-sight integration, dayside limbscans provide an altitude profile at low latitudes (see Figure 2 of Cassidy et al. 2015). They are sensitive to the dependence of the emissions on longitude (local time) and altitude. MASCS detected Mg for the first time (McClintock et al. 2009), and clarified the spatial distribution and seasonal variability of Mg (Merkel et al. 2017), Ca (Burger et al. 2014), and Na (Cassidy et al. 2015; 2016).

XRS

XRS consists of three planet-facing gas-proportional counter (GPC) detectors and a sun-pointing Si-PIN detector within the Solar Assembly for X-rays (SAX). XRS measured the surface (shallower than ~100 μm) abundances of rock-forming elements via planetary X-ray fluorescence. The measured elements can be distinguished based on the energy of incident X-rays and the capabilities of the instrument detectors. The four detectors of XRS cover an energy range of 1–10 keV. 1.25 keV and 3.69 keV Kα lines were observed for Mg and Ca, respectively. Abundance ratio maps of Mg, Ca, Al, S, and Fe to Si were constructed, which clarified the existence of a large Mg-concentrated terrain between 240°E and 320°E longitude in the Northern Hemisphere (Weider et al. 2015). As Ca fluorescence is observable only during solar flares, spatial coverage of the Ca surface abundance is still incomplete. However, it can be seen that Ca enhances around the high-Mg region in the Northern Hemisphere (Nittler et al. 2020).

Analysis

First, we deduced production rates of the exospheric components from the altitude profiles obtained by MASCS. All the dayside limb scan data from 2011 to 2015 were used for the analysis. The column density of exospheric atoms along the line of sight of the spacecraft is approximated by the Chamberlain model (Chamberlain 1963), as follows:

$$N(z) = 2KH\zeta n_0 \, exp\left[\frac{-U+U_0}{k_B T}\right] \quad (1)$$

where z, n_0, k_B, and T are tangential altitude, near-surface density, Boltzmann constant, and temperature, respectively. $2K$ is the ratio of the apparent column density along the line of sight of the spacecraft to the vertical column density, which is approximated by

$$2K \sim \sqrt{\frac{2\pi(R_{Me}+z)}{H(z)}} \quad (2)$$

H, similar to scale height, is defined by the following equation:

$$H(z) = \frac{k_B T (R_{Me}+z)^2}{G M_{Me} M_{atom}} \tag{3}$$

where $G, M_{Me}, M_{atom}, R_{Me}$ are constant of gravitation, the mass of Mercury, the mass of atoms, and the radius of Mercury, respectively. U and U_0 are the potentials of the particles at altitude z and at the surface, respectively, expressed by the following equations:

$$U(z) = -\frac{G M_{Me} M_{atom}}{(R_{Me}+z)} + M_{atom} b \cos Z (R_{Me}+z), U_0 = U(z=0) \tag{4}$$

where b and $\cos Z$ are the solar radiation acceleration, and the cosine of the solar zenith angle, respectively. Although the second term on solar radiation acceleration was ignored in Merkel et al. (2017, 2018), which discussed Mg production rates, we considered it for the sake of generality. In Equation (1),ζ is the partition function calculated as follows:

$$\zeta = \frac{1}{2} + \frac{1}{2} erf\left(\sqrt{\lambda}\right) - \sqrt{\frac{\lambda}{\pi}} e^{-\lambda} - \frac{\sqrt{\lambda_0^2 - \lambda^2}}{2\lambda_0} e^{-\psi}\left(1 + erf\left(\sqrt{\lambda - \psi}\right)\right) + \sqrt{\frac{\lambda(\lambda_0 - \lambda)}{\pi \lambda_0}} e^{-\lambda} \tag{5}$$

where λ, λ_0 are the escape parameters at altitude z and at the surface defined as

$$\lambda(z) = \frac{G M_{Me} M_{atom}}{k_B T (R_{Me}+z)}, \lambda_0 = \lambda(z=0) \tag{6}$$

and ψ is defined as

$$\psi(z) = \frac{\lambda(z)^2}{\lambda(z)+\lambda_0} \tag{7}$$

The Chamberlain model does not consider photoionization. However, photoionization is not effective within the field of view of MASCS ($<10^4$ km), because typical flight scales (the product of the photoionization lifetime and the thermal velocity) of Mg, Ca, and Na at a heliocentric distance of 0.4 au are, respectively, about $10^{6.5}$ km, $10^{4.5}$ km, and 10^5 km.

The apparent column density $N(z)$ in cm^{-2} is derived from the observed radiance $4\pi I$ in Rayleigh from the following conversion formula:

$$N = 10^6 \frac{4\pi I}{g} \tag{8}$$

where g is the probability of solar photon scattering (known as the g-factor). In calculation of g-factor, the values of oscillation strength and solar flux are taken from the National Institutes of Standards and Technology Atomic Spectra Database Lines Form and the LASP Interactive Solar Irradiance Datacenter (LISIRD), respectively. The g-factor is assumed to be uniform for a single TAA assuming that atoms are at rest with respect to Mercury, although it has a standard deviation that is less than approximately 30% owing to the atoms' radial velocity

distribution against the sun. The production rate S is estimated from the product of the near-surface density and first-order moment of velocity distribution function:

$$S = n_0 \int_0^\infty v^2 dv \int_{\theta=\frac{\pi}{2}}^{\theta=0} d\cos\theta \int_0^{2\pi} d\phi f(v,T) v$$
$$= \frac{n_0}{2}\sqrt{\frac{2k_B T}{\pi M_{atom}}} \tag{9}$$

$f(v,T)$ in the equation is the Maxwellian distribution.

We used the Levenberg–Marquardt method to estimate the near-surface density n_0 and temperature T from the altitude profile by fitting with the model profile (Fig. 1). For Mg and Ca, because some data showed an unknown sharp increase in brightness at low altitudes (gray-hatched in the figure), possibly owing to uncorrected scattering from the bright surface, we only used data above 500 km for fitting (Fig. 1a, b). For Na, because it is difficult to precisely evaluate the production rate of higher-energy components owing to the low signal-to-noise ratio of the data or to the limitation of the adopted physical model as pointed out by Cassidy et al. (2015), we used only the production rate of the lower-energy component, which was likely ejected through the PSD (Fig. 1c). Near-surface density, temperature, and production rate of Mg, and temperature of Na obtained in our analysis was consistent with Figure 8 of Merkel et al. (2017) and Figure 8 of Cassidy et al. (2015), respectively. The results for Ca cannot be compared directly with Burger et al. (2014), since they used not the analytical Chamberlain model but a simple numerical model. However, we confirmed that the order of temperature and production rate is consistent with their Fig. 6. To remove the effect of seasonal variability and local time dependence, the production rate at each point was divided by the production rate at the antipodal points at the same TAA, the same local time, and the different Mercury years. Then, we defined a "relative production parameter" Σ_{exos} at the tangential point longitude of ϕ, TAA of α, and local time of h as follows to remove the dependency on TAA and local time:

$$\Sigma_{exos}(\phi,\alpha,h) \equiv log_{10}\left(\frac{S(\phi,\alpha,h)}{S(\phi+\pi,\alpha,h)}\right) \tag{10}$$

A certain longitude comes to the same local time every other Mercury year because of Mercury's 3:2 spin–orbit resonance. Thus, the data of $S(\phi,\alpha,h)$ and $S(\phi+\pi,\alpha,h)$ are obtained from successive Mercury years. When calculating Σ_{exos}, we averaged the production rate S obtained from the data for each local
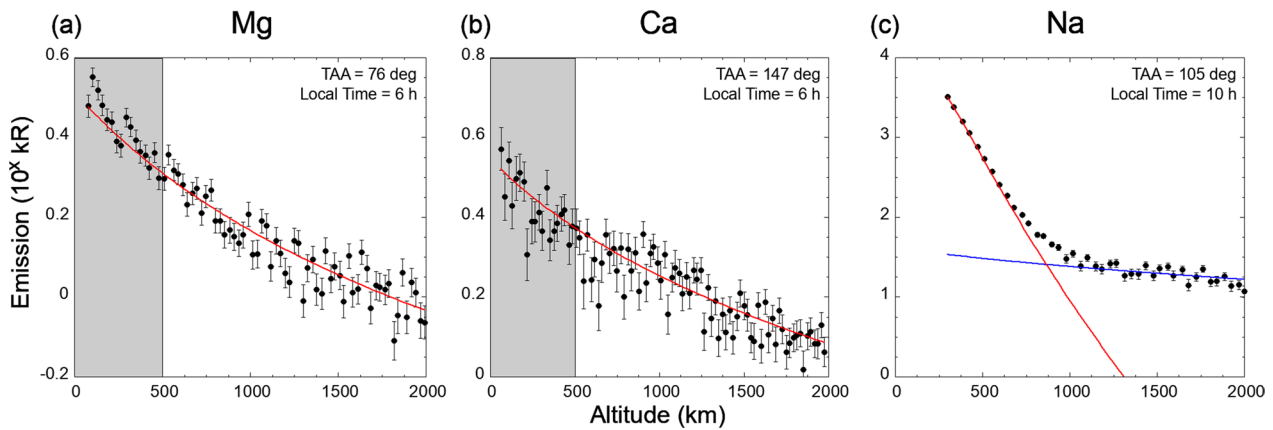
Suzuki *et al. Earth, Planets and Space*   (2023) 75:174

Page 5 of 12

Fig. 1 Fitting to the altitude profile of Mg (**a**), Ca (**b**), and Na (**c**). For Mg and Ca, fitting was performed while ignoring the observations with a tangential altitude lower than 500 km (the gray region). The Na profile was fitted assuming two components: a lower-energy component and a higher-energy component following Cassidy et al. (2015), and only the production rate of the lower-energy component derived from PSD was used. The Levenberg–Marquardt method was used for fitting

time of 2 h and TAA of 4°. Because the seasonal variation and local time dependence are offset by the calculation shown in Eq. (10), $\Sigma_{\text{exos}}(\phi, \alpha, h)$ is expected to strongly depend on the ratio of surface abundance. Note that $\Sigma_{\text{exos}}(\phi, \alpha, h) > 0$ means $S(\phi, \alpha, h) > S(\phi + \pi, \alpha, h)$, and $\Sigma_{\text{exos}}(\phi, \alpha, h) = -\Sigma_{\text{exos}}(\phi + \pi, \alpha, h)$. For Mg and Ca, Pearson product-moment correlation coefficient between $\Sigma_{\text{exos}}(\phi)$ and the surface Mg and Ca abundance ratio defined as $\Sigma_{\text{surf}} \equiv \log_{10}(\sigma(\phi)/\sigma(\phi + \pi))$, is calculated, where σ is the surface density of Mg and Ca around the equator. We used surface Mg and Ca data attached to Nittler et al. (2020). Weighted average and circular moving average whose diameter is 5° were calculated (Fig. 2) as was described in detail in Nittler et al. (2020). Only data at the equator were used in this study. The surface Na density in the Northern Hemisphere was

presumed by Peplowski et al. (2014) based on observations by the Gamma-Ray Spectrometer (GRS) onboard MESSENGER. However, the production rate distribution of the Na exosphere cannot be compared to the surface Na abundance map, because the exosphere data concentrated around the equator do not spread in the latitude direction and the surface data, on the other hand, have little information in the longitudinal direction. Therefore, we continue discussing as much as possible only using exospheric data for the Na case.

Results and discussion

Mg

In Fig. 3a, the relative production parameters of Mg (colored dots) and the surface Mg abundance ratio at the equator (black solid line) as a function of longitude are
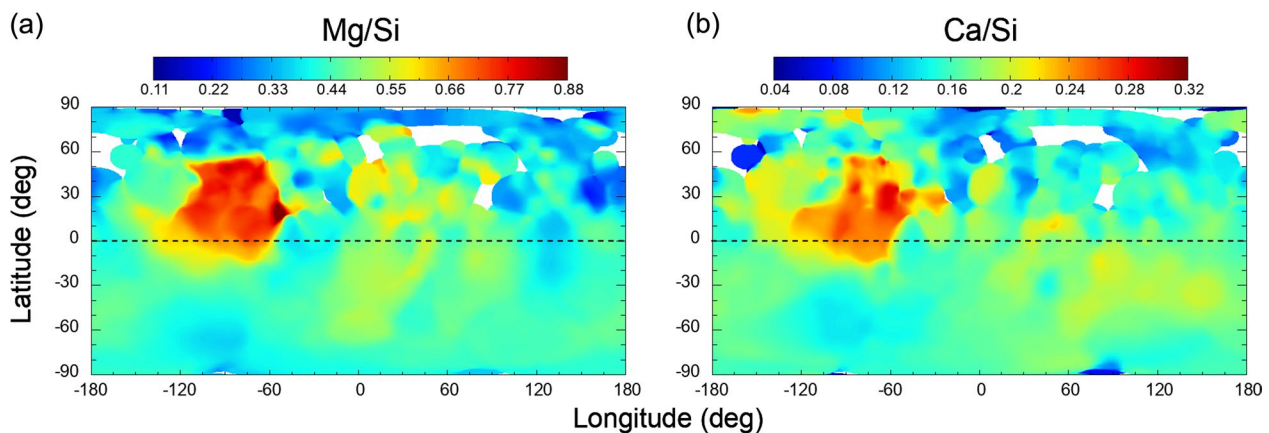

Fig. 2 Surface density distribution of Mg (**a**) and Ca (**b**) deduced from the observations by MESSENGER/XRS. Color scales in (**a**) and (**b**) represent Mg/Si and Ca/Si abundance ratios, respectively

plotted. The second half of the figure is the exact mirror of the first one. The value of error is calculated through the propagation of error of fitting parameters, n_0 and T in Eq. (1). In all the analyses below, including those of Ca and Na, we have systematically removed noisy data with relative error of $S(\phi)/S(\phi + \pi)$ greater than 10%. The correlation coefficient between the production rate ratio and surface abundance ratio was $r = 0.70 \pm 0.17$, with a 95% confidence interval of $0.65 < r < 0.76$. The amount of data used in this study was higher than that used in a previous study (Merkel et al. 2018), which only used local time 06 h data. In addition, calculating the surface Mg abundance ratio in the same way as the production rate of the Mg exosphere enabled statistical tests using the correlation coefficient, which clarified the exosphere–surface correlation for Mg on Mercury. Carefully looking at Fig. 3a, the trend of production rate and that of surface abundance apparently disagree at local time 10 h. Production rate due to MIV is smaller at local time 10 h than at local time 06 and 08 h. Since Mg ejected at local time 06 and 08 is included in the exosphere at local time 10 h due to diffusion, the effect of the enhancement of surface Mg abundance around −100 °E is probably appeared also in the exosphere at local time 10 h.

Ca

The relative production parameters of Ca (colored dots) and the surface Ca abundance ratio at the equator (solid black line) as a function of longitude are plotted in Fig. 3b. The correlation coefficient between the production rate ratio and surface abundance ratio was $r = 0.22 \pm 0.14$, with a 95% confidence interval of $0.12 < r < 0.32$. This result indicates that the local exosphere–surface correlation of Ca is weaker than that of Mg.

The difference between these results is attributed to the difference of their g-factor. Because solar flux at emission wavelength of Ca (422.7 nm) is approximately ten times larger than that of Mg (285.2 nm), g-factor of Ca is also much larger than that of Mg. Consequently, Ca experiences more solar radiation acceleration and is more likely to flow in the tailward direction. To confirm this difference between the two components, we performed three-dimensional Monte Carlo simulations of the trajectories of Mg and Ca atoms in the exosphere. In this model, 10,000 atoms of Mg or Ca are simultaneously ejected only once from −100°E (red arrow in Fig. 4), where Mg and Ca are concentrated.

Ejected atoms move due to the gravity of Mercury and of the sun, and solar radiation pressure. The g-factor is set as a function of the radial velocity with respect to the sun. We assume that Mercury is at the perihelion, or TAA = 0°. Figure 4 shows the line-of-sight column

density of Mg and Ca atoms in 60 min after ejection, seen from the south as MASCS also observed from the south (see Figure 2 of Cassidy et al. 2015). Note that these results do not match observations, since atoms were ejected only once and only from the single point. Because the source of Ca has not yet been identified, our calculation used several energies in the range of 3,000 K to 40,000 K. However, the qualitative results were the same as those in Fig. 4, which shows the case of 20,000 K. These results show that information on the distribution of surface Ca is moved tailward by solar radiation. This makes the exosphere–surface correlation computationally lower, because our method using the Chamberlain model ignores horizontal transport when estimating the production rate.

Na

The relative production parameter of Na (colored dots) as a function of longitude is shown in Fig. 3c. Because Na has a larger amount of data with higher S/N ratio thanks to its brightness, we will discuss using, exclusively, the data with relative error of $S(\phi)/S(\phi + \pi)$ less than 5% instead of 10% (Fig. 5a). The relative production parameter Σ_{exos} is close to 0 at most longitudes, but we can see $\Sigma_{exos} > 0$ in the region from −45°E to 0°E (red box in Fig. 5a). Note again that $\Sigma_{exos}(\phi) > 0$ means that the production rate at the longitude of ϕ (e.g., −45°E) is larger than that at the opposite side whose longitude is $\phi \pm \pi$ (e.g., 135°E). The region from −45°E to 0°E has an especially high maximum temperature of 650 K at the perihelion. Extracting regions whose surface temperature when the data were collected was high (> 550 K), we found that $\Sigma_{exos} > 0$ in the region from −45°E to 45°E (red box in Fig. 5b), which also means that $\Sigma_{exos} < 0$ in the region from 135°E to −135°E.

The cause of $\Sigma_{exos} > 0$ in the region from −45°E to 45°E can be explained well by assuming two forms of Na binding to the surface: physisorption and chemisorption. Similar ideas have often been assumed in Na exosphere models, such as proposed by Leblanc and Johnson (2010). Most of the physisorbed components are composed of Na atoms that re-impacted the surface. Because they are easily ejected through thermal desorption as their binding energy is less than 2.0 eV, the spatial distribution of the exospheric production rates mainly corresponds to the surface temperature. In contrast, the binding energy of chemisorbed Na atoms ranges from 2.6 eV on sodium orthosilicate to 7.9 eV on albite (Morrissey et al. 2022), which implies that chemisorbed Na is distributed depending not only on surface temperature but also on mineral compositions.

A possible scenario is as follows (Fig. 6): when the surface temperature is intermediate (lower than
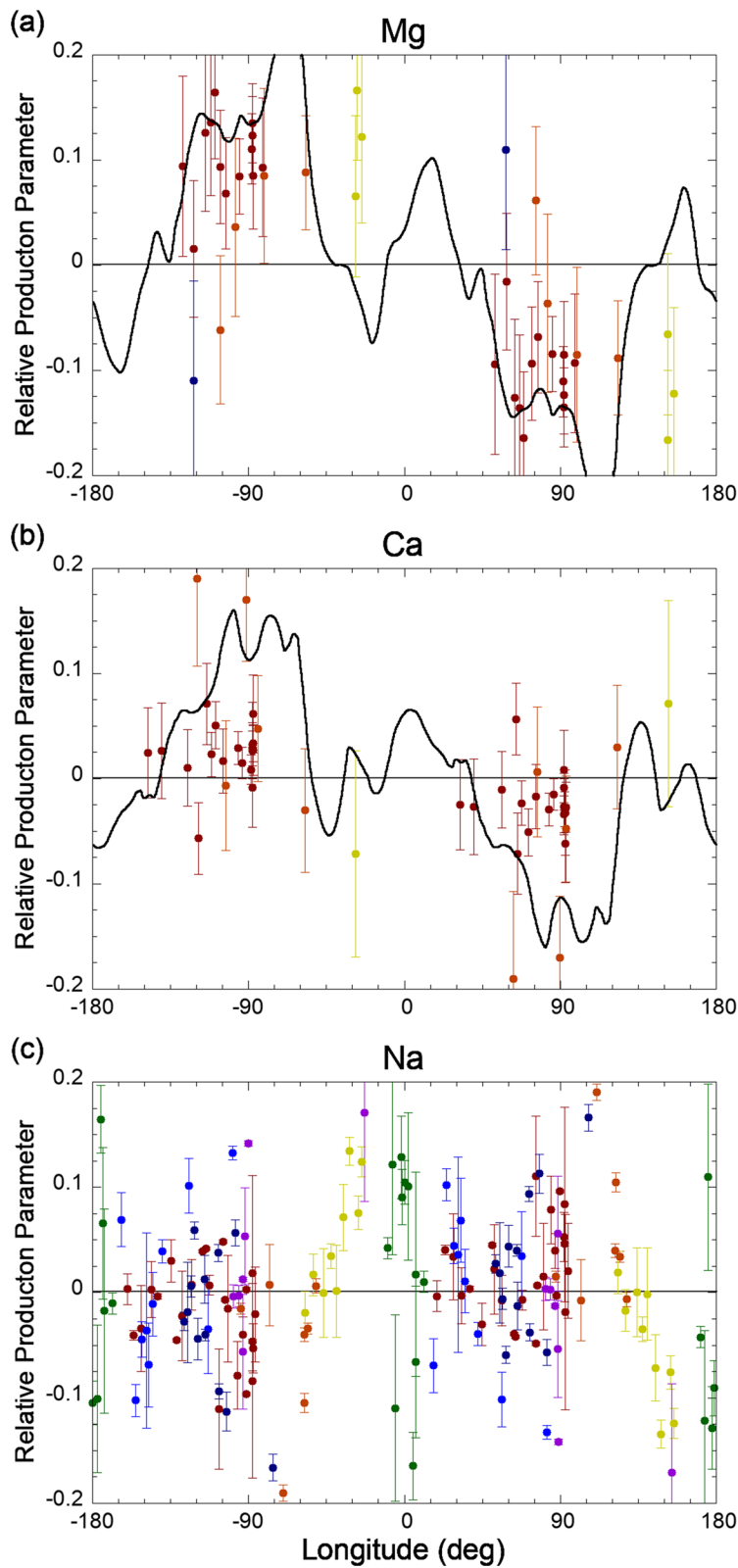
Suzuki *et al. Earth, Planets and Space* (2023) 75:174

Page 7 of 12

Fig. 3 Dependence of the relative production parameter on longitude. Dots are the relative production parameter of the exospheric atoms, which is the common logarithm of the ratio of production rate at a certain longitude to that at an antipodal point. The dot color represents the local time at which the observations were performed. The black solid lines in (**a**) and (**b**) are, respectively, the common logarithm of surface Mg/Si and Ca/Si abundance ratios at a certain longitude to that at an antipodal point
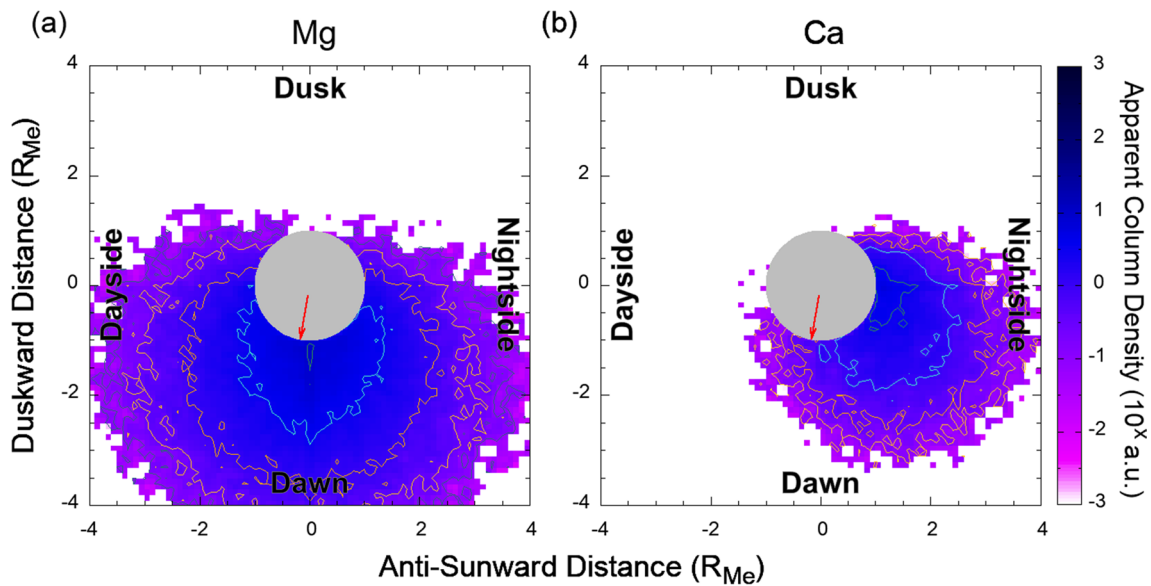
Fig. 4 Distributions of Mg and Ca atoms seen from the south using test particle simulations at perihelion. The color scale, which is displayed on a logarithmic scale, corresponds to the line-of-sight integration of the amount of the exosphere seen from the south as MASCS also observed from the south. The drawn atomic distributions are 60 min after the simultaneous ejection from -100°E (red arrow). Note that the absolute value of the color scale does not have physical meaning. It can be seen that Ca tends to flow in the anti-sunward direction, unlike Mg. Note that these results do not match observations, since atoms were ejected only once and only from the single point
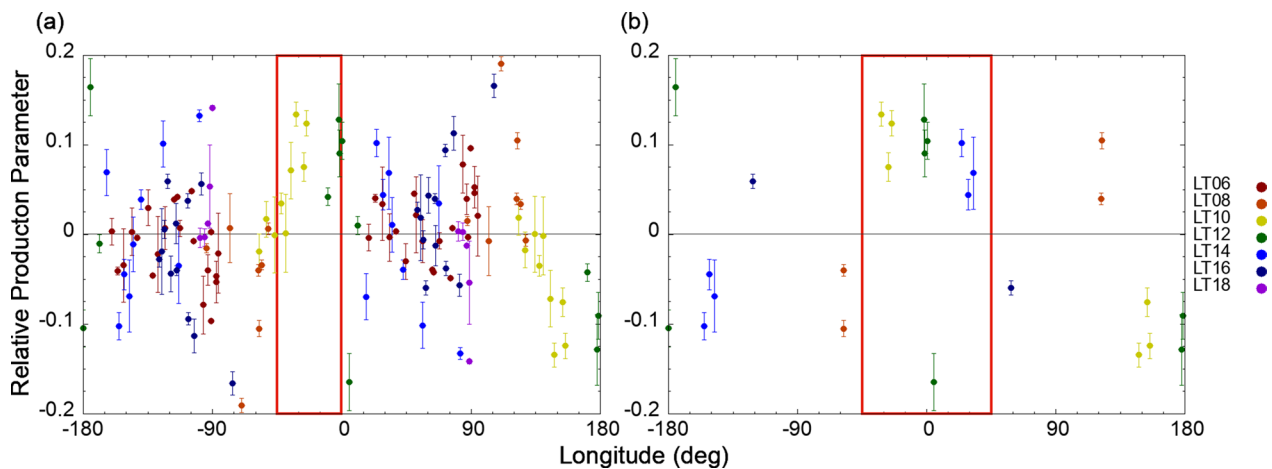

Fig. 5 Dependence of the Na relative production parameter on longitudes. In (**a**), Data with relative error of $S(\varphi)/S(\varphi+\pi)$ is less than 5% are plotted. In (**b**), Data with relative error of $S(\varphi)/S(\varphi+\pi)$ is less than 5% and with temperature above 550 K are plotted. The color of each dot represents the local time when the observations were performed

approximately 500 K), the thermal accommodation layer, which is composed of physisorbed atoms, is not depleted and most of the produced Na exosphere is derived from the physisorbed component. Therefore, the production rate of the exosphere depends mainly on the surface temperature and UV flux. However, in the high-temperature region above 550 K, such as around 0°E (Fig. 7; based on Killen et al. 2004), physisorbed Na atoms are depleted

by thermal desorption, and most of the ejected Na is occupied by chemisorbed atoms. Thus, the production rate of the exosphere begins to depend on geochemical features; that is, an exosphere–surface correlation appears in the high-temperature regions from −45°E to 45°E (and from 135°E to −135°E). Parameters related to thermal desorption, such as binding energy and oscillation frequency, have not been determined well: Hunten
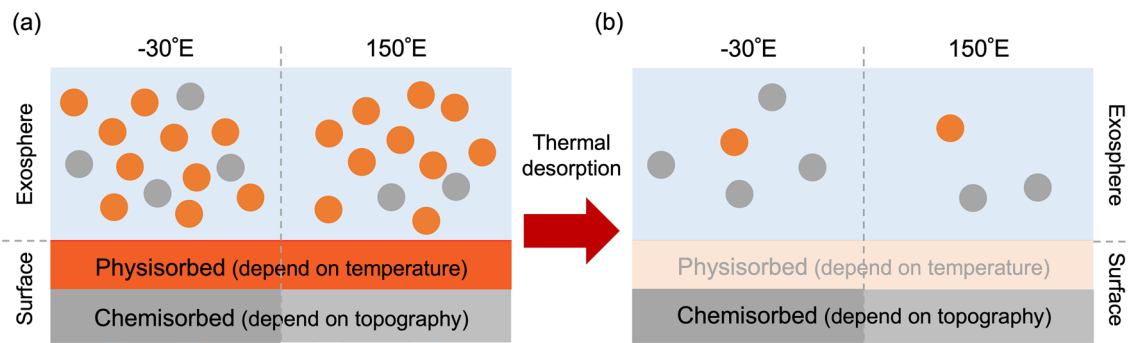
Suzuki *et al. Earth, Planets and Space* (2023) 75:174

Page 9 of 12

Fig. 6 Two-layer scenario of the surface Na. (**a**) At the intermediate temperature of about 500 K, the exosphere mainly consists of physisorbed Na atoms. (**b**) When the surface temperature rises, the physisorbed Na layer is depleted, and chemisorbed Na atoms populate the exosphere. Thus, correlation is considered to appear in the regions with extremely high temperature
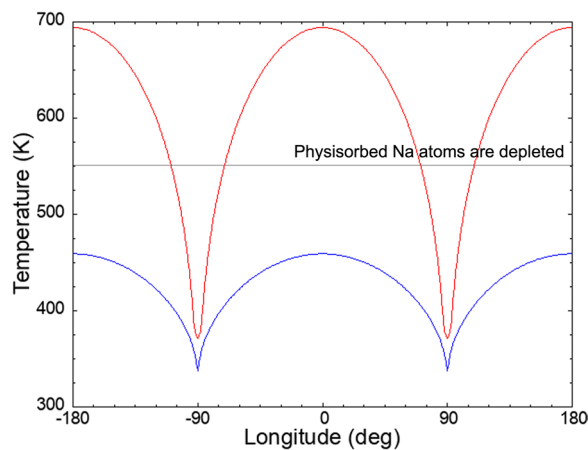

Fig. 7 Surface temperature experienced by each longitude. The red line shows the maximum temperature and the blue line shows the average temperature which each region experiences during Mercury's revolution

and Sprague ([2002]) adopted 1.4 eV and 10^{13} Hz, Leblanc and Johnson ([2010]) used a Gaussian distribution between 1.4 and 2.7 eV with a most probable value of 1.85 eV and 10^9–10^{11} Hz, Suzuki et al., ([2020]) assumed 1.85 eV and 10^{13} Hz (Fig. [8]), and Sarantos and Tsavachidis ([2020]) demonstrated that diffusion makes the energy barrier of the desorption higher. It typically takes approximately 10 min for the thermally desorbed atoms to re-impact the surface estimating from thermal velocity and gravity. For example, if the binding energy is less than 1.85 eV and oscillation frequency is larger than 10^{13} Hz, the desorption rate per 10 min reaches nearly 100% in regions with temperatures above 550 K, which is consistent with our results. Note that the regions with larger production rates do not always correspond to surface composition anomalies, because the solar radiation acceleration of Na is even larger than that of Ca. In addition, the composition

anomaly of the chemisorbed component does not always reflect the volcanic history of Mercury, as it also gradually varies through repeated thermal desorption. We will revisit these points again after observing the surface Na abundance distribution with BepiColombo.

Implication for other components

From the discussion above, low volatility and low solar radiation acceleration are important factors for the local exosphere–surface correlation. The solar radiation acceleration and photoionization lifetimes of some components of Mercury's exosphere are listed in Table [1]. The solar radiation acceleration of the atoms was calculated using the following equation:

$$b = \frac{1}{m_{atom}} \sum_i \frac{h}{\lambda_i} g_i \qquad (11)$$

where m_{atom}, h, λ_i, and g_i are the mass of atoms, Planck constant, wavelength of each emission line, and g-factor, respectively. The g-factor at rest and at 1 au was calculated using values from Killen et al. ([2009]).

In addition, a long photoionization lifetime may be important, although this was not observed in this study. For reference, the photoionization lifetimes derived from Fulle et al. ([2007]) are shown in Table [1]. Atoms with short photoionization lifetimes, such as aluminum, undergo photoionization and reneutralization in a short time. The distribution of exospheric atoms drastically changes during ionization due to the electromagnetic field, which weakens the exosphere–surface correlation. The same analysis as that in this study is required for species with short photoionization lifetimes.

Considering the constants in Table [1], oxygen and sulfur, with small solar radiation acceleration, are expected to have an exosphere–surface correlation on Mercury.

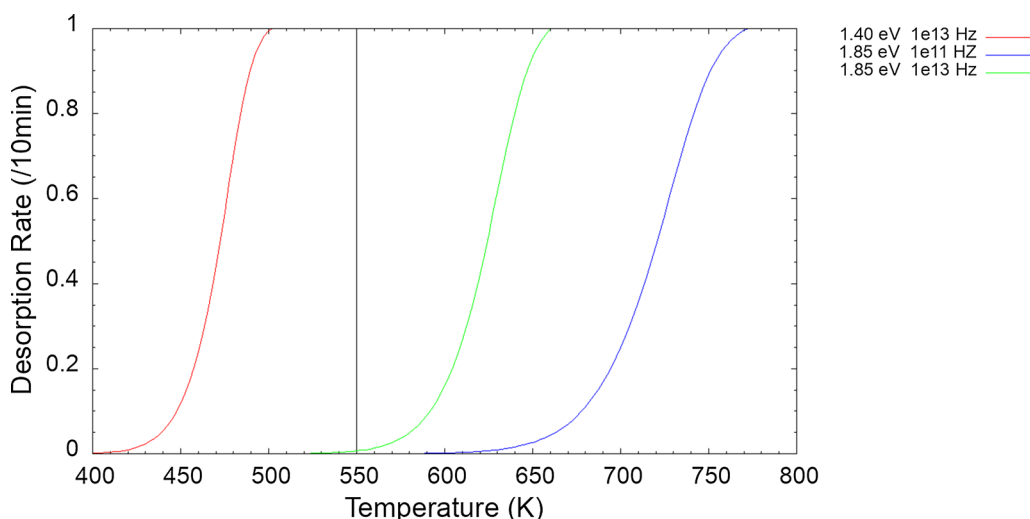Suzuki *et al. Earth, Planets and Space* (2023) 75:174

Page 10 of 12

Fig. 8 Parameter dependence of the thermal desorption rate. The red and green lines use parameter sets adopted by Hunten and Sprague (2002) and Suzuki et al., (2020), respectively. The blue line uses parameters assumed as the most probable values by Leblanc and Johnson (2010). Each line represents the proportion of thermally desorbed Na from the surface

Table 1 Solar radiation acceleration and photoionization lifetime of each atom at 1 au

Component	Solar radiation acceleration at 1 au (m s^{-2})	Photoionization lifetime @1 au (s)	Exosphere–surface correlation on mercury
Na	2.5×10^{-2}	1.9×10^{5}	Weak?
K	2.1×10^{-4}	4.3×10^{4}	Weak?
Mg	1.9×10^{-3}	2.1×10^{6}	Strong
Ca	1.3×10^{-2}	1.4×10^{4}	Weak
O	2.5×10^{-6}	2.0×10^{6}	Strong?
S	4.4×10^{-6}	4.2×10^{5}	Strong?

Because Na and K have larger solar radiation acceleration, a weak exosphere–surface correlation will be observed for Mercury. However, it has been reported that the amount of Na in the lunar exosphere increases above the low-albedo regions (Colaprete et al. 2016) and that of K is enhanced above the KREEP regions (Rosborough et al. 2019). As can be seen from this example, most atoms may have correlation in cooler celestial bodies far from the central star as atoms are hard to volatilize and their solar radiation acceleration is smaller. For exoplanets orbiting stars of different stellar types, atomic species exhibiting exosphere–surface correlation may differ, because their magnitudes of stellar radiation acceleration change.

Conclusion

In celestial bodies with thin atmospheres, atoms are supplied from the surface to the exosphere owing to the effects of the space environment, such as heating, UV radiation, and the impact of micrometeoroids. Thus, the spatial distributions of some components in the exosphere are expected to reflect the distribution of each component on the surface, as well as geological features, such as craters and volcanic terrains. In this study, we verified the existence of a local exosphere–surface correlation on Mercury using observations by MASCS and XRS onboard MESSENGER. As a result, we verified that Mg has a strong correlation, as shown by Merkel et al. (2018), and clarified that Ca has a weak correlation. Based on simple Monte Carlo simulations, we attributed this weak correlation of Ca to effective tailward transportation by solar radiation acceleration. Although Na atoms are easily desorbed thermally, it is possible that a correlation appears in the high-temperature region owing to the rapid depletion of the physisorbed Na layer on the surface. Based on these results, we consider that volatility and solar radiation acceleration control the correlation. S and O may also have an exosphere–surface correlation on Mercury, and it is expected that this correlation will be found in various components on cooler celestial bodies, such as Europa and Ganymede.

The presence or absence of correlation is a very interesting and useful issue, but there has not been enough observational data to discuss this. We hope that observations by the BepiColombo mission (Milillo et al. 2020;

Suzuki *et al. Earth, Planets and Space*   (2023) 75:174

Page 11 of 12

Murakami et al. 2020), launched in 2018 and orbiting Mercury from 2025, will allow us to discuss this issue in more detail. This will provide us with insights into the latitudinal direction—we could only discuss the distribution in the longitudinal direction in this study. The MSASI (Yoshikawa et al. 2010) onboard the Mio spacecraft provides a detailed structure of the Na exosphere. PHEBUS (Quémerais et al. 2020) and SERENA (Orsini et al. 2021) onboard the MPO spacecraft will clarify the distribution of various components in the exosphere, while MERTIS (Hiesinger et al. 2020), MGNS (Mitrofanov et al. 2021), and MIXS (Bunce et al. 2020) onboard the MPO will reveal a wide range of surface material distributions on Mercury. Constraint on binding energy of atoms in surface minerals using numerical models is also necessary for further discussion of exosphere–surface correlation as it affects energy of ejected atoms and exospheric vertical density profile.

Abbreviations

CPS	Charged particle sputtering
GPC	Gas-proportional counter
GRS	Gamma-ray spectrometer
KREEP	Potassium, rare-earth elements, and phosphorous
MASCS	Mercury atmospheric and surface composition spectrometer
MESSENGER	MErcury Surface, Space ENvironment, GEochemistry, and Ranging
MIV	Micro-meteoroid impact vaporization
PSD	Photo-stimulated desorption
SAX	Solar assembly for X-rays
TAA	True anomaly angle
UVVS	Ultraviolet and visible spectrometer
VIRS	Visible and infrared spectrometer
XRS	X-ray spectrometer

Author contributions

KY made substantial contributions to the whole work, including analyzing data, interpretating the acquired results, and revising the manuscript. GM and IY made significant contributions to interpretating of data and revising the manuscript. All authors have approved the submitted version of the manuscript and agreed to be accountable for any part of the work.

Funding

Availability of data and materials

The original data reported in this paper are archived by NASA PDS Geosciences Node (https://pds-geosciences.wustl.edu/missions/messenger/mascs.htm). Oscillation strength of atoms are taken from the National Institutes of Standards and Technology Atomic Spectra Database Lines Form (https://physics.nist.gov/PhysRefData/ASD/lines_form.html). Solar flux are shown in the LASP Interactive Solar Irradiance Datacenter (LISIRD; https://lasp.colorado.edu/lisird/data/sorce_ssi_l3/).

Declarations

Ethics approval and consent to participate

Not applicable.

Consent for publication

Not applicable.

Competing interests

The authors declare that they have no competing interests.

Author details

[1]Institute of Space and Astronautical Science (ISAS), Japan Aerospace Exploration Agency (JAXA), 3-1-1 Yoshinodai, Chuo-Ku, Kanagawa, Sagamihara 252-5210, Japan. [2]Graduate School of Frontier Sciences, The University of Tokyo, 5-1-5 Kashiwa-No-Ha, Chiba, Kashiwa 277-8581, Japan.

References

Bunce EJ, Martindale A, Lindsay S, Muinonen K, Rothery DA, Pearson J, McDonnell I, Thomas C, Thornhill J, Tikkanen T, Feldman C, Huovelin J, Korpela S, Esko E, Lehtolainen A, Treis J, Majewski P, Hilchenbach M, Väisänen T, Luttinen A, Kohout T, Penttilä A, Bridges J, Joy KH, Alcacera-Gil MA, Alibert G, Anand M, Bannister N, Barcelo-Garcia C, Bicknell C, Blake O, Bland P, Butcher G, Cheney A, Christensen U, Crawford T, Crawford IA, Dennerl K, Dougherty M, Drumm P, Fairbend R, Genzer M, Grande M, Hall GP, Hodnett R, Houghton P, Imber S, Kallio E, Lara ML, Margeli AB, Mas-Hesse MJ, Maurice S, Milan S, Millington-Hotze P, Nenonen S, Nittler L, Okada T, Ormö J, Perez-Mercader J, Poyner R, Robert E, Ross D, Pajas-Sanz M, Schyns E, Seguy J, Strüder L, Vaudon N, Viceira-Martín J, Williams H, Willingale D, Yeoman T (2020) The Bepicolombo mercury imaging x-ray spectrometer: science goals, instrument performance and operations. Space Sci Rev 216:126. https://doi.org/10.1007/s11214-020-00750-2
Burger MH, Killen RM, McClintock WE, Merkel AW, Vervack RJ Jr, Cassidy TA, Sarantos M (2014) Seasonal variations in Mercury's dayside calcium exosphere. Icarus 238:51–58. https://doi.org/10.1016/j.icarus.2014.04.049
Cassidy TA, Merkel AW, Burger MH, Sarantos M, Killen RM, McClintock WE, Vervack RJ Jr (2015) Mercury's seasonal sodium exosphere: MESSENGER orbital observations. Icarus 248:547–559. https://doi.org/10.1016/j.icarus.2014.10.037
Cassidy TA, McClintock WE, Killen RM, Sarantos M, Merkel AW, Vervack RJ Jr, Burger MH (2016) A cold-pole enhancement in Mercury's sodium exosphere. Geophys Res Lett 43:11121–11128. https://doi.org/10.1002/2016GL071071
Chamberlain JW (1963) Planetary coronae and atmospheric evaporation. Planet Space Sci 11:911–960. https://doi.org/10.1016/0032-0633(63)90122-3
Christou AA, Killen RM, Burger MH (2015) The meteoroid stream of comet Encke at Mercury: implications for MErcury surface, space ENvironment, GEochemistry, and ranging observations of the exosphere. Geophys Res Lett 42:7311–7318. https://doi.org/10.1002/2015GL065361
Colaprete A, Sarantos M, Wooden DH, Stubbs TJ, Cook AM, Shirley M (2016) How surface composition and meteoroid impacts mediate sodium and potassium in the lunar exosphere. Science 351:249–252. https://doi.org/10.1126/science.aad2380
Fulle M, Leblanc F, Harrison RA, Davis CJ, Eyles CJ, Halain JP, Howard RA, Bockelée-Morvan D, Cremonese G, Scarmato T (2007) Discovery of the atomic iron tail of comet McNaught using the heliospheric imager on STEREO. Astrophys J 661(1):L93–L96. https://doi.org/10.1086/518719
Hiesinger, H., Helbert, J., Alemanno, G., Bauch, K. E., D'Amore, M., Maturilli, A., Morlok, A., Reitze, M. P., Stangarone, C., Sojic, A. N., Varatharajan, I., Weber, I., & the MERTIS Co-I Team (2020) Studying the composition and mineralogy of the hermean surface with the mercury radiometer and thermal infrared spectrometer (MERTIS) for the BepiColombo mission: an update. Space Science Review 216:110. https://doi.org/10.1007/s11214-020-00732-4
Hunten DM, Sprague AL (2002) Diurnal variation of sodium and potassium at Mercury. Meteorit Planet Sci 37:1191–1195. https://doi.org/10.1111/j.1945-5100.2002.tb00888.x
Killen RM, Hahn JM (2015) Impact vaporization as a possible source of Mercury's calcium exosphere. Icarus 250:230–237. https://doi.org/10.1016/j.icarus.2014.11.035

Suzuki *et al. Earth, Planets and Space*   (2023) 75:174

Page 12 of 12

Killen RM, Sarantos, M.m Potter, A. E., & Reiff, P. (2004) Source rates and ion recycling rates for Na and K in Mercury's atmosphere. Icarus 171:1–19. https://doi.org/10.1016/j.icarus.2004.04.007

Killen RM, Shemansky D, Mouawad N (2009) Expected emission from Mercury's exospheric species, and their ultraviolet-visibile signitures. Astrophysics Journal Supplement 181:351–359. https://doi.org/10.1088/0067-0049/181/2/351

Killen RM, Morrissey LS, Burger MH, Vervack RJ Jr, Tucker OJ, Savin DW (2022) The influence of surface binding energy on sputtering in models of the sodium exosphere of Mercury. Planetary Sci J 3:139. https://doi.org/10.3847/PSJ/ac67de

Leblanc F, Johnson RE (2010) Mercury exosphere I. Global circulation model of its sodium component. Icarus 209:280–300. https://doi.org/10.1016/j.icarus.2010.04.020

McClintock WE, Lankton MR (2007) The Mercury atmospheric and surface composition spectrometer for the MESSENGER mission. Space Sci Rev 131:481–521. https://doi.org/10.1007/s11214-007-9264-5

McClintock WE, Vervack RJ Jr, Bradley T, Killen RM, Mouawad N, Sprague AL, Burger MH, Solomon SC, Izenberg NR (2009) MESSENGER observations of Mercury's exosphere: detection of magnesium and distribution of constituents. Science 324(5927):610–613. https://doi.org/10.1126/science.1172525

Merkel AW, Cassidy TA, Vervack RJ Jr, McClintock WE, Sarantos M, Burger MH, Killen RM (2017) Seasonal variations of Mercury's magnesium dayside exosphere from MESSENGER observations. Icarus 281:46–54. https://doi.org/10.1016/j.icarus.2016.08.032

Merkel AW, Vervack RJ Jr, Killen RM, Cassidy TA, McClintock WE, Nittler LR, Burger MH (2018) Evidence connecting Mercury's magnesium exosphere to its magnesium-rich surface terrane. Geophys Res Lett 45:6790–6797. https://doi.org/10.1029/2018GL078407

Milillo A, Fujimoto M, Murakami G, Benkhoff J, Zender J, Aizawa S, Dósa M, Griton L, Heyner D, Ho G, Imber SM, Jia X, Karlsson T, Killen RM, Laurenza M, Lindsay ST, McKenna-Lawlor S, Mura A, Raines JM, Rothery DA, André N, Baumjohann W, Berezhnoy A, Bourdin PA, Bunce EJ, Califano F, Deca J, de la Fuente S, Dong C, Grava C, Fatemi S, Henri P, Ivanovski SL, Jackson BV, James M, Kallio E, Kasaba Y, Kilpua E, Kobayashi M, Langlais B, Leblanc F, Lhotka C, Mangano V, Martindale A, Massetti S, Masters A, Morooka M, Narita Y, Oliveira JS, Odstrcil D, Orsini S, Pelizzo MG, Plainaki C, Plaschke F, Sahraoui F, Seki K, Slavin JA, Vainio R, Wurz P, Barabash S, Carr CM, Delcourt D, Glassmeier K-H, Grande M, Hirahara M, Huovelin J, Korablev O, Kojima H, Lichtenegger H, Livi S, Matsuoka A, Moissl R, Moncuquet M, Muinonen K, Quèmerais E, Saito Y, Yagitani S, Yoshikawa I, Wahlund J-E (2020) investigating Mercury's environment with the two-spacecraft BepiColombo mission. Sp Sci Rev 216:93. https://doi.org/10.1007/s11214-020-00712-8

Mitrofanov IG, Kozyrev AS, Lisov DI, Litvak ML, Malakhov AA, Mokrousov MI, Benkhoff J, Owens A, Schulz R, Quarati F (2021) The Mercury gamma-ray and neutron spectrometer (MGNS) onboard the mercury planetary orbiter of the BepiColombo mission: design updates and first measurements in space. Space Sci Rev 217:67. https://doi.org/10.1007/s11214-021-00842-7

Morrissey LS, Tucker OJ, Killen RM, Nakhla S, Savin DW (2022) Solar wind ion sputtering of sodium from silicates using molecular dynamics calculations of surface binding energies. Astrophys J Lett 925(1):L6. https://doi.org/10.3847/2041-8213/ac42d8

Mura A, Wurz P, Lichtenegger HIM, Schleicher H, Lammer H, Delcourt D, Milillo A, Orsini S, Massetti S, Lhodachenko ML (2009) The sodium exosphere of Mercury: comparison between observations during Mercury's transit and model results. Icarus 200:1–11. https://doi.org/10.1016/j.icarus.2008.11.014

Murakami G, Hayakawa H, Ogawa H, Matsuda S, Seki T, Kasaba Y, Saito Y, Yoshikawa I, Kobayashi M, Baumjohann W, Matsuoka A, Kojima H, Yagitani S, Moncuquet M, Wahlund J-E, Delcourt D, Hirahara M, Barabash S, Korablev O, Fujimoto M (2020) Mio—first comprehensive exploration of Mercury's space environment: mission overview. Space Science Review 216:113. https://doi.org/10.1007/s11214-020-00733-3

Nittler LR, Frank EA, Weider SZ, Crapster-Pregont E, Vorburger A, Starr RD, Solomon SC (2020) Global major-element maps of Mercury from four years of MESSENGER X-ray spectrometer observations. Icarus 345:113716. https://doi.org/10.1016/j.icarus.2020.113716

Orsini S, Livi SA, Lichtenegger H, Barabash S, Milillo A, De Angelis E, Phillips M, Laky G, Wieser M, Olivieri A, Plainaki C, Ho G, Killen RM, Slavin JA, Wurz P, Berthelier J-J, Dandouras I, Kallio E, McKenna-Lawlor S, Szalai S, Torkar K, Vaisberg O, Allegrini F, Daglis IA, Dong C, Escoubet CP, Fatemi S, Fränz M, Ivanovski S, Krupp N, Lammer H, Leblanc F, Mangano V, Mura A, Nilsson H, Raines JM, Rispoli R, Sarantos M, Smith HT, Szego K, Aronica A, Camozzi F, Di Lellis AM, Fremuth G, Giner F, Gurnee R, Hayes J, Jeszenszky H, Tominetti F, Trantham B, Balaz J, Baumjohann W, Brienza D, Bührke U, Bush MD, Cantatore M, Cibella S, Colasanti L, Cremonese G, Cremonesi L, D'Alessandro M, Delcourt D, Delva M, Desai M, Fama M, Ferris M, Fischer H, Gaggero A, Gamborino D, Garnier P, Gibson WC, Goldstein R, Grande M, Grishin V, Haggerty D, Holmström M, Horvath I, Hsieh K-C, Jacques A, Johnson RE, Kazakov A, Kecskemety K, Krüger H, Kürbisch C, Lazzarotto F, Leblanc F, Leichtfried M, Leoni R, Loose A, Maschietti D, Massetti S, Mattioli F, Miller G, Moissenko D, Morbidini A, Noschese R, Nuccilli F, Nunez C, Paschalidis N, Persyn S, Piazza D, Oja M, Ryno J, Schmidt W, Scheer JA, Shestakov A, Shuvalov S, Seki K, Selci S, Smith K, Sordini R, Svensson J, Szalai L, Toublanc D, Urdiales C, Varsani A, Vertolli N, Wallner R, Wahlstroem P, Wilson P, Zampieri S (2021) SERENA: particle instrument suite for determining the sun-Mercury interaction from BepiColombo. Space Science Review 217:11. https://doi.org/10.1007/s11214-020-00787-3

Peplowski PN, Evans LG, Stockstill-Cahill KR, Lawrence DJ, Goldsten JO, McCoy TJ, Nittler LR, Solomon SC, Sprague AL, Starr RD, Weider SZ (2014) Enhanced sodium abundance in Mercury's north polar region revealed by the MESSENGER Gamma-Ray Spectrometer. Icarus 228:86–95. https://doi.org/10.1016/j.icarus.2013.09.007

Quémerais E, Chaufray J-Y, Koutroumpa D, Leblanc F, Reberac A, Lustrement B, Montaron C, Mariscal J-F, Rouanet N, Yoshikawa I, Murakami G, Yoshioka K, Korablev O, Belyaev D, Pelizzo MG, Corso A, Zuppella P (2020) PHEBUS on Bepi-Colombo: post-launch update and instrument performance. Space Science Review 216:67. https://doi.org/10.1007/s11214-020-00695-6

Rosborough SA, Oliversen RJ, Mierkiewicz EJ, Sarantos M, Robertson SD, Kuruppuaratchi DCP, Derr NJ, Gallant MA, Roesler FL (2019) High-resolution potassium observations of the lunar exosphere. Geophys Res Lett 46:6964–6971. https://doi.org/10.1029/2019GL083022

Sarantos M, Tsavachidis S (2020) The boundary of alkali surface bound-ary exospheres of mercury and the moon. Geophysical Res Lett 47(16):e2020GL088930. https://doi.org/10.1029/2020GL088930

Schlemm CE II, Starr RD, Ho GC, Bechtold KE, Hamilton SA, Boldt JD, Boynton WV, Bradley W, Fraeman ME, Gold RE, Goldsten JO, Hayes JR, Jaskulek SE, Rossano E, Rumpf RA, Schaefer ED, Strohbehn K, Shelton RG, Thompson RE, Trombka, j. I., & Williams, B. D. (2007) The X-ray spectrometer on the MESSENGER spacecraft. In: Domingue DL, Russell CT (eds) The Messenger Mission to Mercury. New York, NY, Springer. https://doi.org/10.1007/978-0-387-77214-1_11

Suzuki Y, Yoshioka K, Murakami G, Yoshikawa I (2020) Seasonal variability of Mercury's sodium exosphere deduced from MESSENGER data and numerical simulation. Journal of Geophysical Research Planets. 125:e2020JE006472. https://doi.org/10.1029/2020JE006472

Weider SZ, Nittler LR, Starr RD, Crapster-Pregont EJ, Peplowski PN, Denevi BW, Head JW, Byrne PK, Hauck SA II, Ebel DS, Solomon SC (2015) Evidence for geochemical terranes on Mercury: global mapping of major elements with MESSENGER's X-ray spectrometer. Earth Planet Sci Lett 416:109–120. https://doi.org/10.1016/j.epsl.2015.01.023

Yoshikawa I, Korablev O, Kameda S, Rees D, Nozawa H, Okano S, Gnedykh V, Kottsov V, Yoshioka K, Murakami G, Ezawa F, Cremonese G (2010) The Mercury sodium atmospheric spectral imager for the MMO spacecraft of Bepi-Colombo. Planet Space Sci 58(1–2):224–237. https://doi.org/10.1016/j.pss.2008.07.008

Publisher's Note